Article:
Shan, J. orcid.org/0000-0001-5946-6460, Huang, Y. orcid.org/0000-0002-1220-6896 and Jiang, W. orcid.org/0000-0002-8062-8329 (2025) Efficient Bi-TiO2 photocatalytic materials for asphalt applications: Synthesis, characterization, and NO degradation performance. Journal of Cleaner Production, 518. 145947. ISSN 0959-6526

https://doi.org/10.1016/j.jclepro.2025.145947

Original article

Efficient Bi-TiO_2 Photocatalytic Materials for Asphalt Applications: Synthesis, Characterization, and NO Degradation Performance

Jinhuan Shan[a, b], Yue Huang[c], Wei Jiang[a, b, *]

a. Key Laboratory for Special Area Highway Engineering of Ministry of Education, Chang'an University, Xi'an 710064, China

b. School of Highway, Chang'an University, Xi'an 710064, China

c. Institute for Transport Studies, University of Leeds, Leeds LS2 9JT, UK

*Corresponding author: Wei Jiang, jiangwei@chd.edu.cn

Abstract: Rapid urbanization and increasing vehicular emissions have intensified nitrogen oxide (NO) pollution, posing serious environmental and health risks. Photocatalytic materials, such as TiO_2, offer a sustainable solution for pollutant degradation; however, their practical efficiency is constrained by a wide band gap (~3.2 eV) and high electron-hole recombination rates, limiting visible-light activity. This study addresses these challenges by synthesizing Bi-doped TiO_2 nanoparticles via sol-gel and hydrothermal methods, incorporating them into asphalt, and evaluating their photocatalytic performance in degrading both gaseous (nitric oxide, NO) and aqueous (methyl orange, MO) pollutants under UV and visible light. Comprehensive material characterization (XRD, SEM, TEM, XPS, UV-vis DRS, VB-XPS, BET) revealed that hydrothermally synthesized TiO_2 exhibited nearly twice the BET surface area (~194 vs. 107 m^2/g), larger crystallite size (~14 vs. 10 nm), and smaller particle size (~20-30 nm vs. 25-45 nm) compared to sol-gel TiO_2, leading to enhanced photocatalytic activity. Optimal Bi doping (3-4%) effectively reduced the TiO_2 band gap from ~2.8-2.85 eV to ~2.3-2.5 eV, improving visible-light absorption. Density Functional Theory (DFT) calculations confirmed that Bi doping introduced impurity states that facilitated band gap narrowing, while excessive oxygen vacancies diminished visible-light activity by suppressing these states. Photocatalytic evaluations demonstrated that Bi-doped TiO_2 achieved up to 90.8% NO degradation under UV light and 77.6% under visible light, while also significantly enhancing MO degradation efficiency compared to undoped TiO_2. These findings highlight the potential of Bi-doped TiO_2-modified asphalt as a multifunctional material for sustainable urban air pollution mitigation with enhanced photocatalytic stability and efficiency under real-world conditions.

Keywords: Photocatalytic pavement; Asphalt; Titanium dioxide; Air pollution; Bismuth-doping

1. Introduction

The global expansion of vehicular traffic, driven by economic growth and technological advancements, has led to a significant increase in traffic-related pollution. It contributes to environmental pollution through two primary pathways: exhaust emissions and non-exhaust emissions (He et al., 2024; He & Jiang, 2024; Jiang et al., 2024). Non-exhaust pollution primarily arises from road surface and tire wear, generating particulate matter and microplastics that accumulate in the environment. Mitigating this type of pollution requires improving material durability, such as enhancing road pavement resistance and optimizing tire composition to reduce wear (Baghitabar et al., 2023). Exhaust emissions, on the other hand, pose a more complex challenge due to their widespread dispersion in the atmosphere. This pollution poses severe health risks, with both short- and long-term exposure linked to increased incidences of cardiopulmonary diseases, respiratory ailments, and metabolic disorders, potentially reducing human life expectancy(Debelu et al., 2024; Slomski, 2018; van Veldhoven et al., 2019). Current strategies to mitigate vehicle exhaust pollution encompass pre-engine approaches (e.g., fuel quality enhancement), in-engine improvements (focusing on fuel efficiency), and post-engine measures (such as exhaust filtration and degradation) (Gao et al., 2017). Despite policy interventions in various nations, including vehicle purchase and usage restrictions, and incentives for new energy vehicles, the continuous growth of global urbanization often counteracts these air pollution reduction efforts (Dylla et al., 2013).

Semiconductor photocatalysts have emerged as a promising solution to address both environmental pollution and the global energy crisis (Ahmad et al., 2023; Eftekharipour et al., 2023). These materials, when exposed to light, generate electron-hole pairs capable of participating in redox reactions, leading to the degradation of organic pollutants, CO_2 reduction, hydrogen production, and removal of hazardous substances(Chen et al., 2020; Gul et al., 2020; Khan et al., 2020; Sayed et al., 2022; Wei et al., 2020). The application of photocatalytic materials in self-cleaning buildings,

road coatings, and photocatalytic pavements has become a focal point of research. Roads, with their extensive surface area and direct exposure to vehicle exhaust, present an ideal environment for capturing and degrading pollutants, offering a more effective solution compared to building surfaces and road auxiliary facilities (X. Li et al., 2023). While nano-TiO_2 is widely utilized in environmental applications, its wide bandgap and rapid electron-hole recombination limit its efficiency under visible light, constraining its effectiveness in road environments (Gatou et al., 2024). To enhance its photocatalytic performance, researchers have developed modified nano-TiO_2 materials through methods such as doping, deposition, and composite formation, significantly improving TiO_2's photocatalytic activity. Researchers have improved the photocatalytic activity of titanium dioxide through various modification techniques, including doping (Narindri Rara Winayu et al., 2022), deposition (Sangpour et al., 2010), and the formation of composites (Hou et al., 2007; H. Wang et al., 2007). Among these, bismuth doping (Bi-TiO_2) has attracted significant attention due to its ability to shift the photocatalytic response of TiO_2 into the visible light region and to suppress the recombination of photogenerated electron-hole pairs, thereby improving its effectiveness in applications including organic pollutant degradation, antimicrobial treatment, and photocathode design (Barkouch et al., 2023; Estrada-Flores et al., 2022; Mishra et al., 2024).

Despite the promising performance of Bi-TiO_2 materials, a critical knowledge gap remains concerning the influence of synthesis methods on their photocatalytic behavior. Different synthesis techniques-such as sol-gel and hydrothermal methods-can substantially affect key physicochemical properties of the catalyst, including crystallinity, crystal structure, morphology, and defect density. These structural differences, in turn, govern charge carrier dynamics and ultimately impact photocatalytic efficiency. Although numerous studies have reported the synthesis and application of Bi-doped TiO_2 (Alimard et al., 2024; L. Ma et al., 2025; Tolan et al., 2023), few have systematically investigated how different synthesis approaches

influence material performance through both experimental characterization and theoretical simulations. In particular, limited work has integrated first-principles (DFT) calculations with experimental validation to elucidate the mechanistic origins of performance variations. This lack of a comprehensive understanding hampers the ability to tailor Bi-TiO_2 properties for specific photocatalytic applications.

In parallel with the above materials-focused perspective, another important challenge exists in the practical application of Bi-TiO_2 in environmental remediation. To address traffic emission degradation, initial efforts focused on incorporating TiO_2 into concrete materials, such as concrete blocks (Poon & Cheung, 2007; Hüsken et al., 2009) and cement concrete pavements (Ballari et al., 2010a, 2010b; Dylla et al., 2010; M. M. Hassan et al., 2010; Xu et al., 2020). As asphalt pavements became more prevalent in urban areas with high traffic emissions, research into photocatalytic asphalt pavements intensified (T. Wang et al., 2025). Techniques such as spray coating (M. Hassan et al., 2013) and epoxy-bonded TiO_2 (D. Wang et al., 2016, 2017) were explored, alongside studies aimed at enhancing photocatalytic activity using TiO_2 composites (Jin et al., 2018; Liu et al., 2015) and doped TiO_2 materials (Cao et al., 2017; Hu et al., 2021). there remains a significant gap in its application in photocatalytic pavement materials. Specifically, research on Bi-TiO_2-modified asphalt is still limited, particularly with respect to the comparative characterization of different synthesis methods and the analysis of photocatalytic efficiency at both the material and modified asphalt levels. The preparation methods and physicochemical properties of photocatalysts play a crucial role in determining their photocatalytic performance. However, many current studies merely focus on the direct application of photocatalysts in asphalt without systematically distinguishing how different preparation methods and their physicochemical properties affect the photocatalytic performance. Additionally, there is a lack of in-depth analysis at the molecular level to fully understand the mechanisms behind photocatalysis.

Therefore, this study addresses two critical gaps: (1) the lack of mechanistic understanding of how synthesis methods affect the properties and photocatalytic efficiency of Bi-TiO_2, and (2) the limited application-oriented research on Bi-TiO_2-modified asphalt for air pollution mitigation. By integrating theoretical modeling with systematic material characterization and functional testing in asphalt systems, this work provides a comprehensive framework for optimizing photocatalyst design and deployment in environmental applications. To address these challenges, this study investigates Bi-doped TiO_2 photocatalysts synthesized via sol-gel and hydrothermal methods, aiming to clarify the impact of synthesis conditions on material structure and photocatalytic performance. Both theoretical modeling (via DFT) and experimental analyses (XRD, SEM, TEM, XPS, UV-Vis DRS, VB-XPS, BET) were employed to systematically examine structure-property relationships. Furthermore, these Bi-TiO_2 materials were integrated into asphalt to evaluate their photocatalytic efficiency in degrading NO under both UV and visible light conditions. The key contributions of this study are:

(1) Mechanistic insight into how synthesis methods affect the crystallinity, morphology, surface area, and electronic structure of Bi-TiO_2 photocatalysts, supported by both experimental data and DFT simulations.

(2) Quantitative comparison of the photocatalytic activity of Bi-TiO_2 synthesized by different methods for degrading MO and NO under UV and visible light.

(3) Demonstration of practical applicability through the incorporation of optimized Bi-TiO_2 into asphalt composites, revealing strong potential for real-world air pollution mitigation.

(4) Establishment of a comprehensive framework combining material design, multiscale characterization, and photocatalytic validation, to guide future development of visible-light-responsive photocatalysts for urban environmental applications.

2. Materials and methods

2.1 Catalyst preparation

All chemicals and reagents used in this study were analytical grade and used without further purification. Bi-doped TiO_2 photocatalysts were synthesized by the sol-gel method and hydrothermal method. For comparison, bare TiO_2 photocatalysts were also prepared by the same method. The specific synthesis steps are shown in Fig. 1.

Sol-gel method: In a typical synthesis process, 4.8 g citric acid was dissolved in 100 mL of 1M HNO_3 by stirring for 30 min. Then a certain amount of Bismuth nitrate pentahydrate was added to the above solution by stirring for 30 min at room temperature. The obtained solution was denoted as solution A. 8.8 mL of Tetrabutyl titanate (TBT) was added to 17.5 mL of anhydrous alcohol by stirring for 30 min forming the solution B. Then, solution A was added into the solution B drop by drop and stirred for 2 h forming the solution C. Solution C was aged for 24 h at room temperature and dried at 85 °C for 12 h, before being dried in a vacuum drying chamber at 120 °C for 2 h. The powder was ground before being heated to 450 °C in a muffle furnace for 2 h. The synthesized Bi-doped TiO_2 samples were labelled based on the synthesis method and Bi doping concentration. Samples prepared via the sol-gel method were designated as S_x, where x represents the Bi/Ti molar ratio (e.g., S0, S1.0, S2.0, S3.0, S4.0 correspond to Bi/Ti ratios of 0%, 1.0%, 2.0%, 3.0%, and 4.0%, respectively). Similarly, hydrothermally synthesized samples were labelled as H_x, where x indicates the Bi/Ti ratio (e.g., H0, H1.0, H2.0, H3.0, H4.0 for 0%, 1.0%, 2.0%, 3.0%, and 4.0%, respectively).

Hydrothermal method: The method of preparing solution C was the same as the sol-gel method. Then, the as-prepared solution C was subjected to a hydrothermal reaction in a hydrothermal reaction vessel at 120 °C for 8 h, and then the solution cooled at room temperature. After the reaction, the as-obtained solution was treated in the same way as the sol-gel method. The obtained samples were named as H*x*, where *x* was the mole ratio of Bi to TiO_2 (%) (x = 1, 2, 3, 4 and 5).

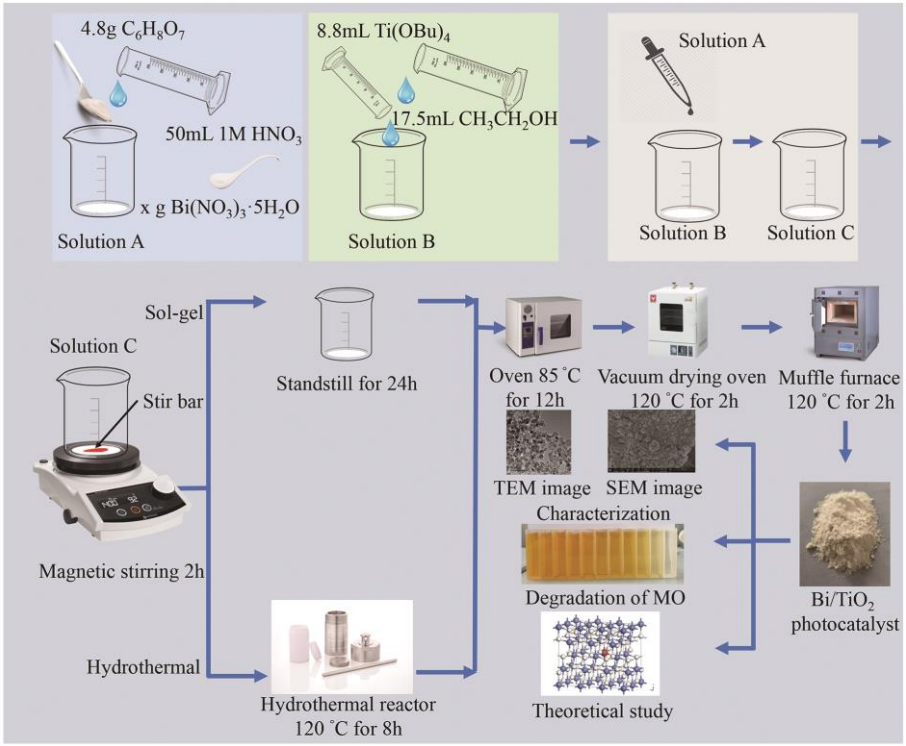

Fig. 1 The photocatalysts preparation process (Sol-gel and hydrothermal method)

2.2 Catalyst characterization

To comprehensively characterize the physicochemical properties of the photocatalysts, a suite of analytical techniques was employed. X-ray diffraction (XRD) (Bruker D8 Advance, Cu Kα radiation, λ = 0.15406 nm) was used to determine the crystalline phase composition, crystallinity, and estimate crystallite size via the Scherrer equation. Scanning electron microscopy (SEM) (FEI Verios 460), coupled with energy dispersive X-ray spectroscopy (EDX), was utilized to investigate the surface morphology, particle size distribution, and elemental composition of the samples. Transmission electron microscopy (TEM) (FEI Tecnai G2 F20) provided high-resolution images for analyzing internal microstructures, lattice fringes, and defect states at the nanoscale.

X-ray photoelectron spectroscopy (XPS) and valence band XPS (VB-XPS) (Thermo Fisher ESCALAB 250Xi) were used to probe the chemical states, bonding environments, and valence band edge positions, offering insight into defect levels and band alignment. Brunauer–Emmett–Teller (BET) surface area and porosity

measurements were carried out using a Micromeritics ASAP 2020 instrument, which enabled quantitative assessment of specific surface area, pore volume, and pore size distribution. Ultraviolet-visible diffuse reflectance spectroscopy (UV-vis DRS) (Shimadzu UV-2600) was performed to determine the light absorption behavior and calculate the band gap energies via Tauc plots.

2.3 Calculation method

All the density functional theory (DFT) calculations were performed using the Cambridge Serial Total Energy Package (CASTEP) code. The generalized gradient approximation (GGA) with the Perdew-Burke-Ernzerhof (PBE) function was used for the exchange-correlation effects. The core and valence electron interactions were modeled by on-the-fly generation (OGFT) ultrasoft pseudopotentials with an energy cutoff of 630.0 eV.

In the calculations, oxygen vacancy systems were constructed using different sizes ($2 \times 2 \times 2$ and $3 \times 2 \times 1$) anatase supercells with an oxygen vacancy site substituted for a O atom, where TiO_{2-x} system corresponds to oxygen vacancy concentration of x = 0.03125 and 0.04167, and doping systems were also constructed using these anatase supercells with a Bi atom substituted for a Ti atom (Fig. 2), where $Ti_{1-x}Bi_xO_2$ system corresponds to Bi doping concentration of x=0.04167 and 0.03125 (which were approximate to the experimental doping concentration). Bi-doped TiO_2 with oxygen vacancy was also constructed with a Bi atom and an oxygen vacancy marked as $Ti_{1-x}Bi_xO_{2-x}$ (x=0.04167). In order to evaluate the reasonability of the simulation methodology, pure anatase supercells were also calculated. Different Monkhorst-Pack scheme k-point grid samplings were set for the Brillouin zone ($3 \times 3 \times 1$ and $2 \times 3 \times 3$) with the self-consistent field of 5.0×10^{-7} eV/atom. During geometry optimization, the quality of convergence tolerance was set to ultra-fine, where the tolerance of energy, maximum force, maximum stress and maximum displacement convergences were set to 5.0×10^{-6} eV/atom, 0.01 eV/Å, 0.02 Gpa and 5.0×10^{-4} Å. After the geometry

optimization was finished, the band structures were calculated using the same settings as geometry optimization.

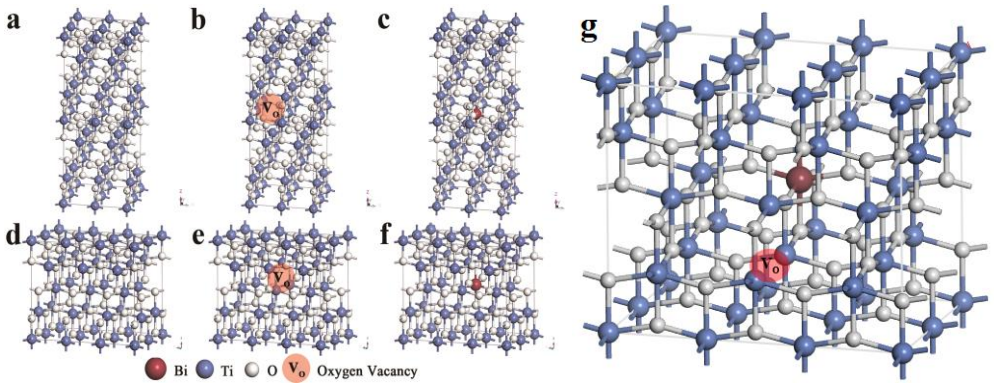

Fig. 2 Structural model of (a) undoped TiO_2 (2 × 2 × 2), (b) undoped TiO_2 with oxygen vacancy (2 × 2 × 2), (c) Bi-doped TiO_2 (2 × 2 × 2), (d) undoped TiO_2 (3 × 2 × 1), (e) undoped TiO_2 with oxygen vacancy (3 × 2 × 1), (f) Bi-doped TiO_2 (3 × 2 × 1) and (g) Bi-doped TiO_2 with oxygen vacancy (3 × 2 × 1)

2.4 Photocatalytic activity test

The photocatalytic experiments of Bi doped TiO_2 were conducted with the degradation of Methyl Orange (MO) under UV and visible light. In each case, 0.1 g of photocatalyst was dispersed in 100 mL of MO solution (20 mg/L). A 300 W Xe lamp (BBZM-I) was used as the light source. A UV-cut filter ($\lambda > 420$ nm) was applied to obtain visible light. For UV irradiation, a UVA bandpass filter (315-400 nm) was used to selectively transmit UVA light. The solution was stirred in dark for 60 min to reach the equilibrium of adsorption and desorption before the light was on. The distance between the solution and light was 30 cm. The sample was removed from the solution after a certain time internals and then centrifuged at 3000 rpm for 10 min to remove the remaining residue of the catalysts. The corresponding concentration of MO was examined at 466 nm with the 721 visible spectrophotometer (Shanghai Jinghua Group Co., Ltd, China).

The photocatalytic efficiency of the photocatalyst-modified asphalt (90# asphalt) was evaluated by the degradation of nitric oxide (NO) with a specific concentration. The experiment adopted a self-made automobile exhaust gas decomposition experiment chamber, which is connected with a gas tank and automobile exhaust gas analysis

instrument (as shown in Fig. 3). The gas analyzer used in this study was the PTM600 Portable Multi-Gas Analyzer, with detailed specifications listed in Table 1. The light source setup for the NO degradation experiment was the same as described for the MO degradation test. The reaction chamber had dimensions of 400 × 400 × 200 mm, with a quartz glass top to ensure excellent light transmission, maintaining optimal illumination conditions during the experiment. The remaining chamber structure was made of acrylic, which is lightweight, easy to install, and cost-effective. The use of transparent acrylic also allowed for real-time observation of the degradation process inside the chamber. The distance between the light source and the sample was set at 25 cm to ensure consistent and uniform irradiation. A humidity controller, a recycle gas blower and a temperature controller were arranged in the box to ensure the stability of the experimental conditions. Firstly, the photocatalyst with 1% of the asphalt quality was put into 140 °C asphalt and stirred evenly by high shear emulsifier with 3000 r/min for 30 min. The uniformly stirred modified asphalt was then introduced into the sample tray with a diameter of 10.5 cm, and the thickness of sample was 1.00 ± 0.05 mm. The sample tray was then put into the chamber in the dark. Turn on the recycle gas blower, adjust the temperature to 25 °C, and close the chamber. Then the NO gas was introduced, and the gas analyzer monitored the gas concentration. When the gas concentration reaches 250 ppm, close the gas valve. Turn on the light and the gas concentration were record by the gas analyzer at regular intervals.

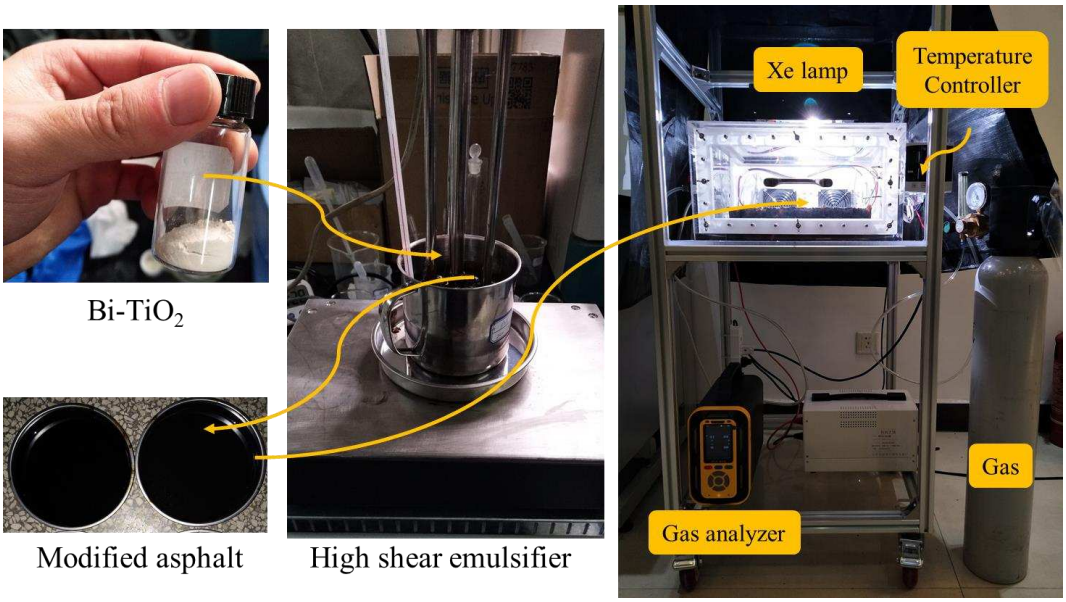

Fig. 3 Exhaust gas decomposition experiment chamber

Table 1 Specifications of the PTM600 Portable Multi-Gas Analyzer

Specification	Details
Detection Range	0 ~ 1000 ppm
Resolution	0.1 ppm
Response Time	T90 ⩽ 20 seconds
Recovery Time	⩽ 30 seconds
Working Conditions	Temperature: -40°C ~ +70°C Humidity: ⩽10 ~ 95% RH
Detection Mode	Built-in pumped type with 800 ml/min flow rate
Accuracy	⩽±2% F.S.
Dimensions & Weight	230×210×120 mm, 2.5 kg

3. Result

3.1 XRD analysis

The crystalline phase of S0, S1.0, S2.0, S3.0, S4.0, S5.0, H0, H1.0, H2.0, H3.0, H4.0 and H5.0 are shown in Fig. 4. The peaks at around 2θ = 25.30°, 37.78°, 48.01°, 53.94°, 55.05° and 62.68° are consistent with anatase phase (PDF No. 65-5714). There are no significant changes as the amount of Bi increased, which may be due to the small amount of Bi compared to the large amount of TiO_2. The phases of $Bi_4Ti_3O_{12}$ orthorhombic structure were also detected at around 2θ = 30.06° (PDF No. 35-0795). The peaks of $Bi_4Ti_3O_{12}$ at around 30.19° are clearer with the increase of the moral ratio of Bi/Ti. The intensities of characteristic XRD peaks decrease as the increase of the

moral ratio of Bi/Ti, which indicates that the crystallinity and crystallite size of samples decreased. The crystallinity and crystallite size of samples synthesized by different methods (sol-gel method and hydrothermal method) also showed a marked difference. Samples synthesized by hydrothermal method had better crystallinity and bigger crystallite size than that synthesized by the sol-gel method based on the X-ray diffraction (XRD) peaks intensities and peaks width at half maximum height.

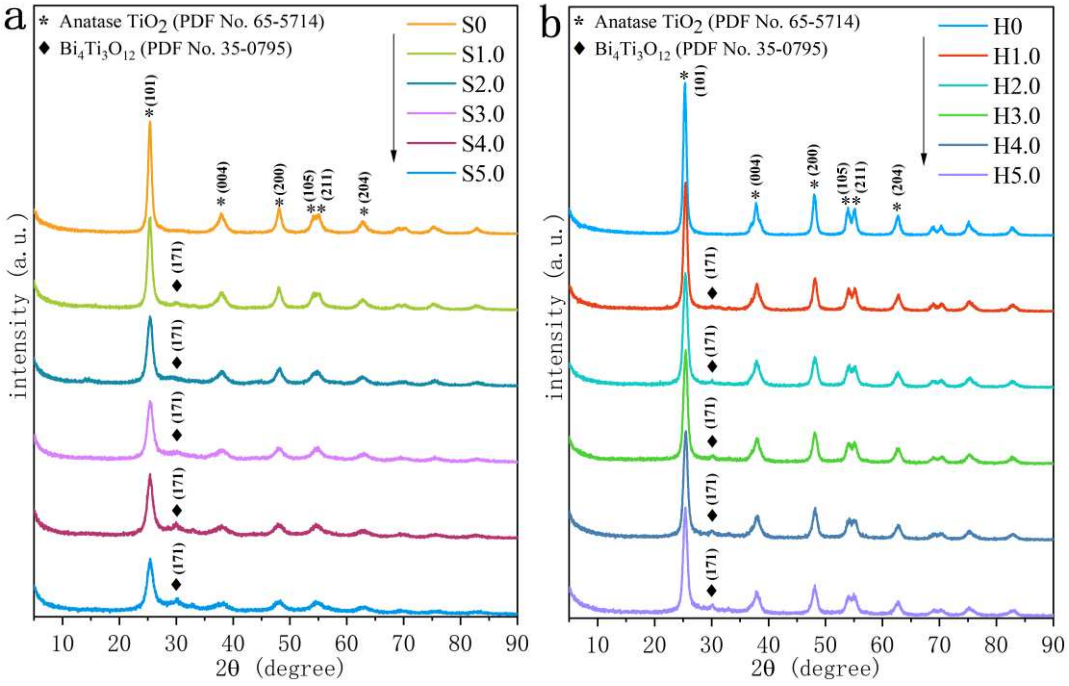

Fig. 4 XRD patterns of samples of different moral ratio of Bi/Ti synthesized by sol-gel method (a) and hydrothermal method (b)

The crystallite sizes of S0, S3.0, S4.0, H0, H3.0 and H4.0 were shown in Table 2, which were calculated of the anatase (101) reflection at the peak of 2θ = 25.30° using Scherrer's formula:

$$L = K\lambda / (\beta cos\theta) \quad (1)$$

where K is a constant (K = 0.89), λ is the wavelength of X-ray radiation ($\lambda_{Cu\ K\alpha}$ = 0.15406 nm), β is the line width at half maximum height (FWHM), and θ is the diffracting angle (Komaraiah et al., 2019). It can be seen that the examples synthesized by the sol-gel method had the crystallite size between 8 nm to 10nm, while the samples synthesized by the hydrothermal method held the size between 10 nm to 15 nm.

Table 2 The crystalline size, particle size, surface area, pore size and pore volume of samples

samples	Crystalline size (nm)		Particle size (nm)	Surface area	Pore size	Pore volume
	XRD	TEM	SEM image	(m^2/g)	(nm)	(cm^3/g)
S0	10.0	/	25~45	106.55	6.9352	0.2099
S3.0	8.5	8~10	40~80	109.38	7.0386	0.1959
S4.0	8.4	/	50~100	107.65	7.2307	0.1976
H0	14.5	/	20~30	193.96	8.03 85	0.4322
H3.0	10.5	9~12	30~50	162.92	9.4159	0.4216
H4.0	10.7	/	30~50	145.63	10.6141	0.4150

3.2 SEM and SEM-EDX analysis

The scanning electron microscope (SEM) was used to study the morphology of samples. SEM images of samples of S0, S3.0, S4.0, H0, H3.0 and H4.0 are shown in Fig. 5. The ImageJ software was used to measure the particle size of samples and the results were displayed in Table 2. From Fig. 5, it can be seen that the particle size increased with the increase of moral ratio of Bi/Ti. The particles synthesized by the hydrothermal method had a smaller particle size than those synthesized by the sol-gel method. The samples of H0 displayed the smallest particle size (about 20 nm ~ 30nm), while S4.0 displayed the largest particle size (about 50 nm ~ 80 nm). What's more, it should be noted that the shape of samples synthesized by the hydrothermal method displayed a relatively uniform sphere, while that synthesized by sol-gel method were more irregular.

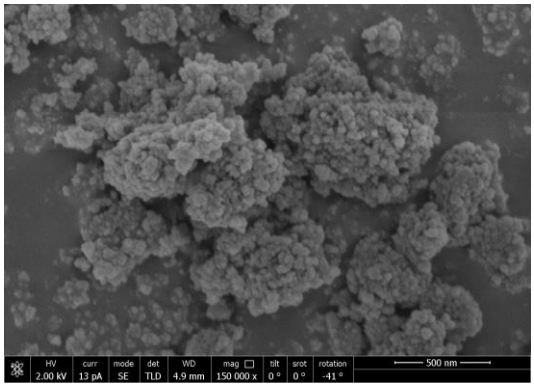

(a) S0

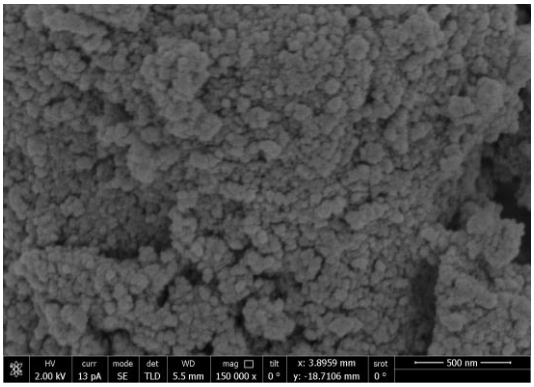

(d) H0

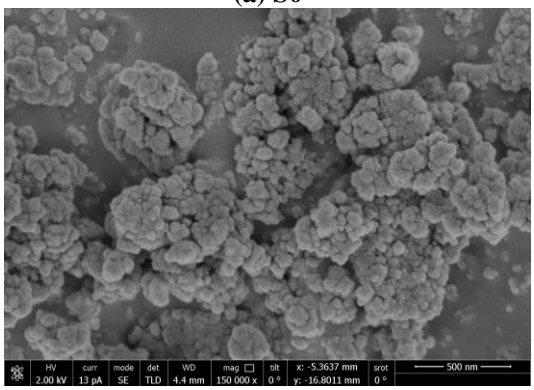

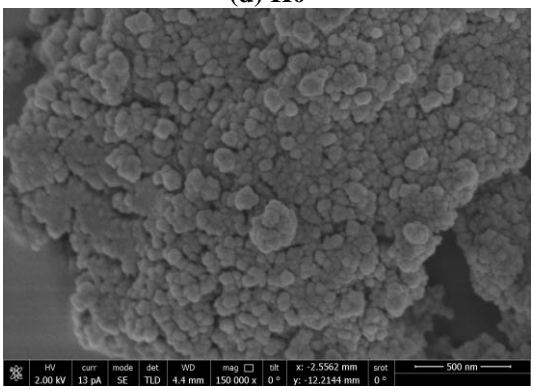

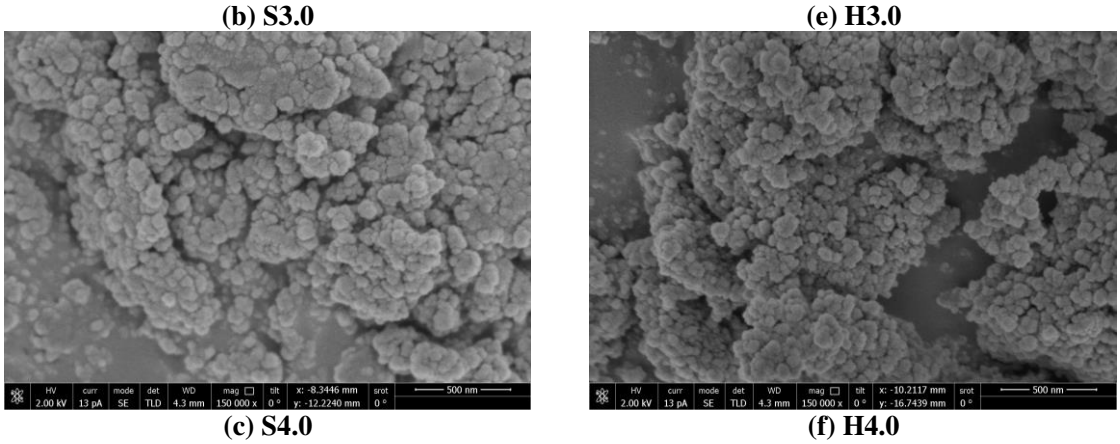

Fig. 5 SEM images of samples: S0 (a), S3.0 (b), S4.0 (c), H0 (d), H3.0 (e) and H4.0 (f)

Energy dispersive X-ray (EDX) was used to characterize the quantitative elemental composition of the samples of S3.0 and H3.0 (Fig. 6). From Fig. 6, it can be seen that the atomic ratio of Ti:O was about 1:2 which agreed well with TiO_2. However, the atomic ratio of Bi:Ti was smaller than the theoretical ratio (3.0%), which was 1.8% and 1.9% respectively. The concentration of Bi of samples synthesized by the hydrothermal method was higher than that synthesized by the sol-gel method, probably because of the high temperature and pressure environment of the hydrothermal method, which made the chemical reactions more violent.

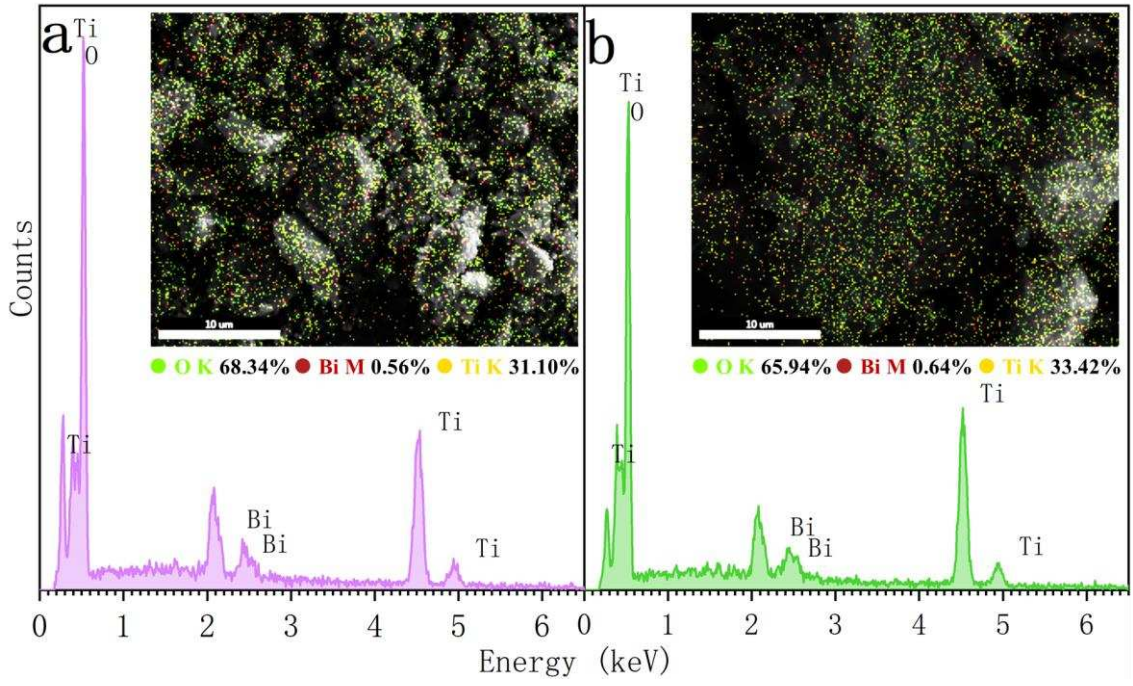

Fig. 6 EDX spectrums of S3.0 (a) and H3.0 (b)

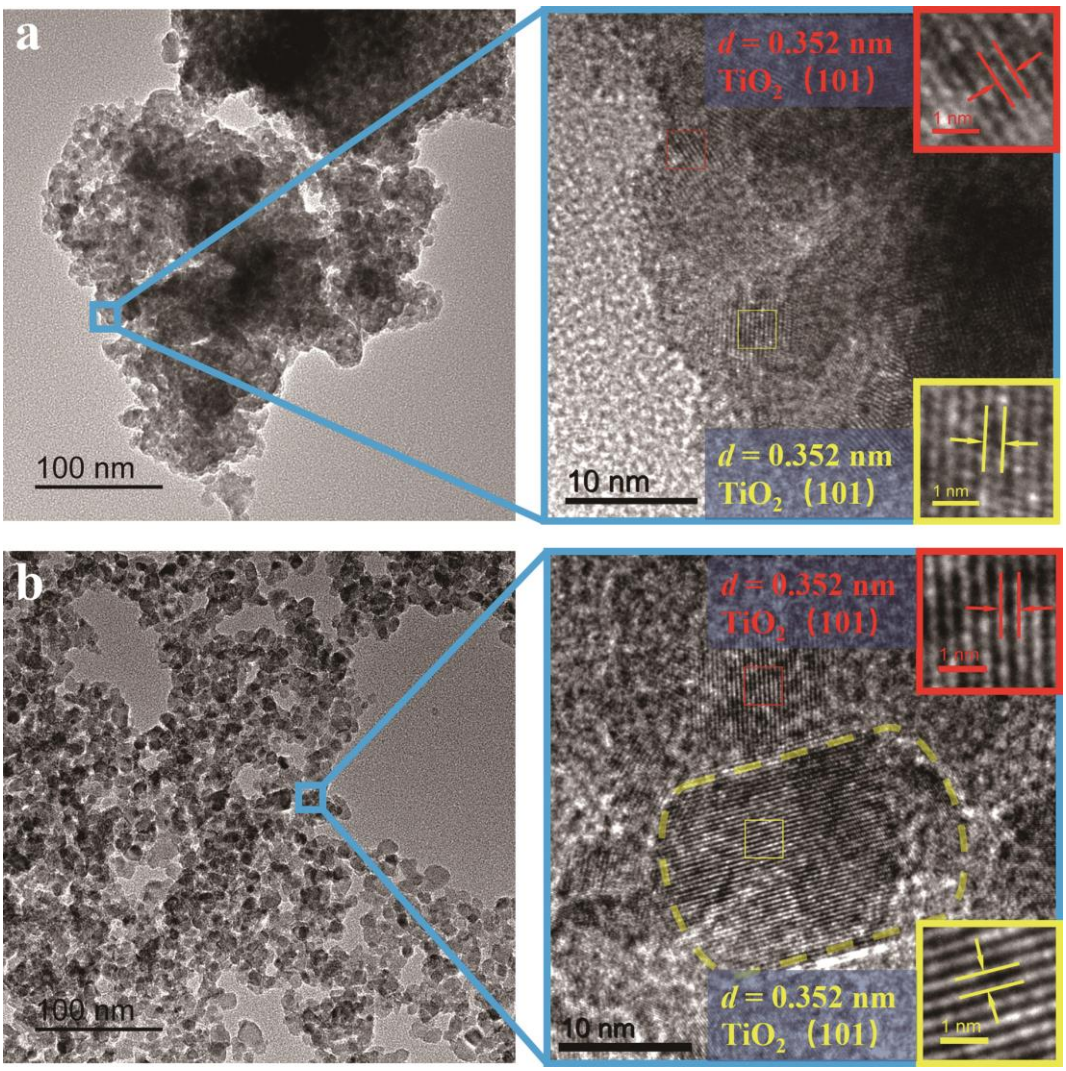

Fig. 7. TEM and HRTEM images of S3.0 (a) and H3.0 (b)

3.3 TEM and HRTEM analysis

The microstructure and morphology of S3.0 and H3.0 were characterized by transmission electron microscopy (TEM) and high-Resolution TEM (HRTEM) as Fig. 7 shows. All the S3.0 and H3.0 particles displayed the lattice fringes with an interplanar distance of 0.352 nm correspond to the (101) crystal plane of anatase TiO_2. But there is no crystal plane of $Bi_4Ti_3O_{12}$ because of the low number of crystals and the wide dispersion. The crystal sizes of S3.0 and H3.0 were measured by the ImageJ software showing in the Table 2. The size of S3.0 was smaller than H3.0 which was well consistent with the XRD analysis. However, it needs to be noted that the TEM images of S3.0 (Fig. 7(a)) shows that the particles aggregated and it is hard to find individual and complete grains, revealing that the samples synthesized by sol-gel method have

more disorder amorphous layers and crystal defects which have great influence on the photoactivity of semiconductor. The particles of H3.0 slightly aggregated but still can be clearly seen. From HRTEM image of Fig. 7 (b), the (101) crystal plane of anatase TiO_2 was clearly displayed revealing the well crystallinity of samples synthesized by hydrothermal method.

3.4 XPS analysis

X-ray photoelectron spectroscopy measurements (XPS) were used to identify the surface element chemical states and the high-resolution XPS spectrums of samples S0, S3.0, H0 and H3.0 are shown in Fig. 8. Fig. 8(a) shows a high-resolution XPS spectrum of Ti 2p with two picks at around 464.4 eV and 458.6 eV which were assigned to the Ti $2p_{1/2}$ and Ti $2p_{3/2}$ of Ti^{4+}. After doped Bi^{3+}, Ti 2p binding energies shift to the low side by about 0.15 eV of sample S3.0 and about 0.1 eV of sample H3.0, which indicates that chemical states of Ti^{4+} can be lowered with the doping of Bi and sol-gel method has more influence on the chemical states of Ti^{4+}. In Fig. 8(b), the peaks at 164.6 eV and 159.3 eV are assigned to Bi $4f_{5/2}$ and Bi $4f_{7/2}$ of Bi^{3+}, and the peaks at 162.7 eV and 157.5 eV are assigned to Bi $4f_{5/2}$ and Bi $4f_{7/2}$ of Bi^0(J. Ma et al., 2012).

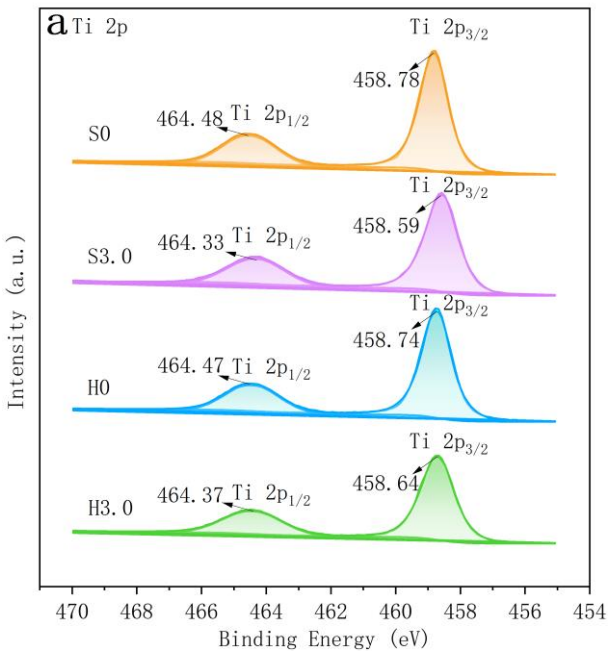

(a) Ti 2p

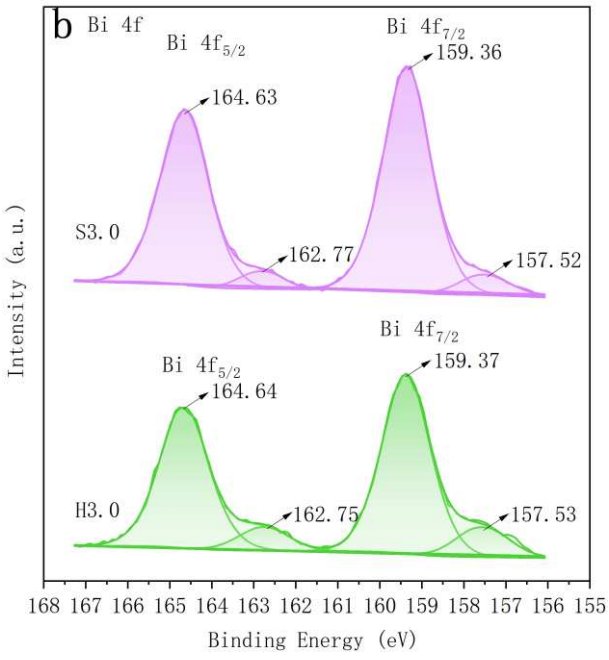

(d) Bi 4f

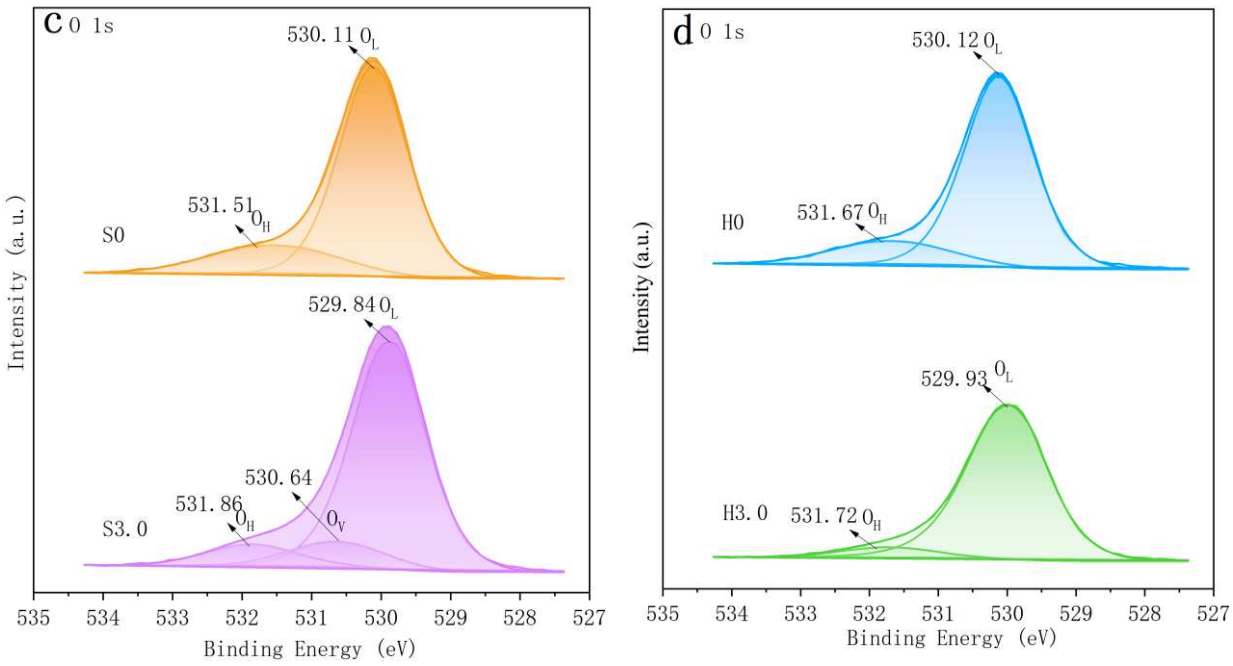

(b) O 1s **(e) O 1s**

Fig. 8 High-resolution XPS spectrums of Ti 2p (a), Bi 4f (b), and O 1s of sample S0 (c) and S3.0, and O 1s of sample H0 and H3.0 (d)

Fig. 8(c) and (d) show the high-resolution XPS spectrums of O 1s. All of the samples can be fitted into at least two peaks at around 530.0 eV and 531.7 eV which can be assigned to crystal lattice oxygen (O_L) and hydroxyl oxygen (O_H). However, the sample S3.0 has another peak at around 530.6 eV which may be assigned to oxygen vacancies (Qi et al., 2019).

3.5 UV-vis DRS and VB-XPS analysis

UV-vis diffuse reflectance spectra (UV-vis DRS) was used to examine the absorbance properties of the sample S0, S3.0, S4.0, H0, H3.0 and H4.0 which is shown in Fig. 9. The sample S0 and H0 had a sharp decrease around 425 nm due to the band gap transition, while the sample S3.0 S4.0, H3.0 and H4.0 can be observed red shift in the absorption light edge and had a long tail which is beneficial to expand the absorption range. The samples S3.0 and S4.0 had a higher tail than samples H3.0 and H4.0, which is probably caused by the more lattice defects, such as oxygen vacancies (Lv et al., 2009), which agree with the results of XPS of sample S3.0. It should be noted that in the UV region, the sample H0 can absorb the most ultraviolet light than other samples

but the absorbance value of the sample S0 is smaller than other samples, which may significantly influence the photoactivity under UV light.

The optical band gap energy (*E*g) of the samples S0, S3.0, S4.0, H0, H3.0 and H4.0 evaluated by Tauc plot equation(2) (Adhikary et al., 2015) is shown in the inset picture of Fig. 9.

$$(\alpha h\nu)^{1/2} = K(h\nu - Eg) \quad (1)$$

Where α is the optical absorption coefficient; h is the Planck's constant; ν is the incident radiation frequency; K is constant; Eg is gap energy. The direct band gap energy can be obtained by the intercept at the *x*-axis, which is shown in the inset picture Fig. 9. The band gap energies of bare TiO_2 are around 2.85 eV of the sample S0 and 2.8 eV of the sample H0 which is lower than the value (3.20 eV) of other experiments which may be caused by the absence of defects (L. Li et al., 2014; Nowotny et al., 2015; Rahman et al., 2015; Samsudin & Abd Hamid, 2017). The band gap energies of S3.0, S4.0, H3.0 and H4.0 were also calculated by the Tauc plot equation, 2.31 eV, 2.32 eV, 2.48 eV and 2.39 eV respectively which is lower than that of bare TiO_2 indicating that the presence of Bi ion can considerably reduce the band gap. It should be noted that the band gap energy of the samples synthesized by sol-gel method is slightly lower than that synthesized by hydrothermal method, which is probably because the samples synthesized by the sol-gel method has more defects which also can be deduced by the higher tail of UV-vis DRS spectra. Interestingly, in the UV region, the sample H0 has the highest absorption but the sample S0 has the lowest absorption, which could be explained by the dense surface layer of samples synthesized by the sol-gel method according to the small surface area (Table 2) and stacked crystal.

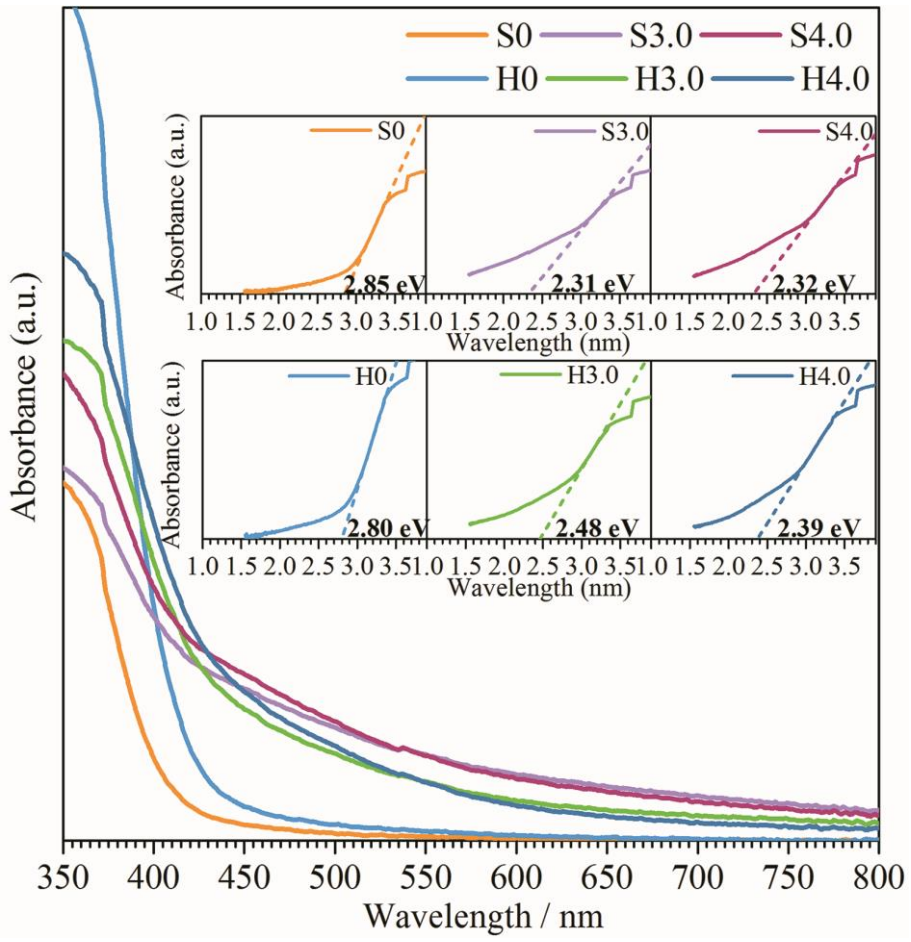

Fig. 9 UV-vis DRS spectra of the samples S0, S3.0, S4.0, H0, H3.0 and H4.0 (Inset image is band gap of samples calculated by the Tauc plot equation)

The valance band of the sample S0, H0, S3.0 and H3.0 can be calculated by the intercept at the *x*-axis of VB-XPS spectra, as shown in Fig. 10. The valance bands (VBs) of the sample S0 and S3.0 are the same at around 2.60 eV under the Fermi energy level. The VBs of H0 and H3.0 are increased about 0.1 eV and 0.15 eV respectively because of the introduction of Bi ions which can slightly change the crystal structure and thus the band structure shifts. This can be explained by two key factors: Bi doping primarily affects the conduction band minimum (CBM) by introducing impurity states, leading to band gap reduction, while the valence band maximum (VBM) remains relatively stable. The sol-gel method introduces more oxygen vacancies, as observed in the UV-vis DRS spectra, which alters the electronic structure and counteracts the expected VBM shift caused by Bi doping.

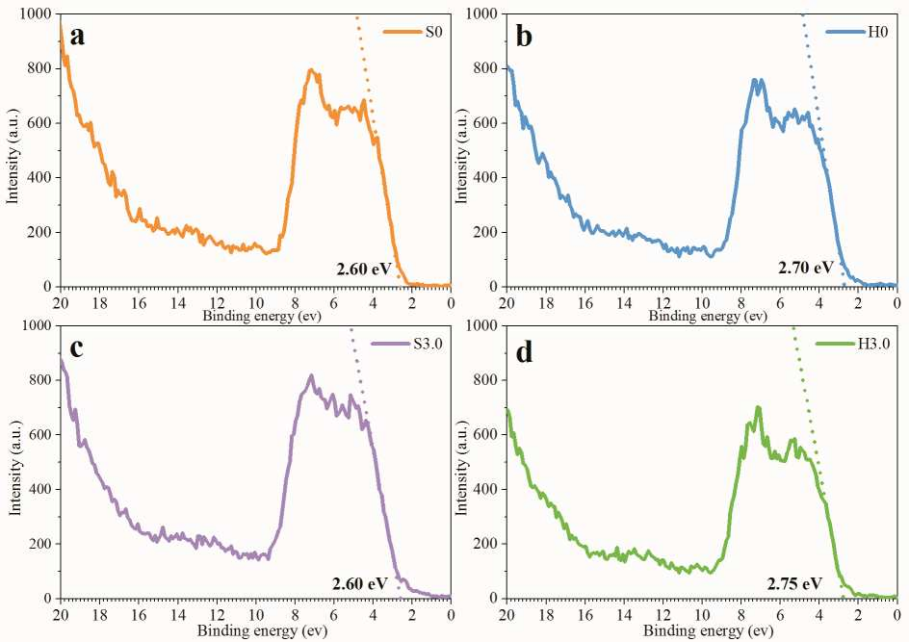

Fig. 10 VB-XPS image of the sample S0, H0, S3.0 and H3.0

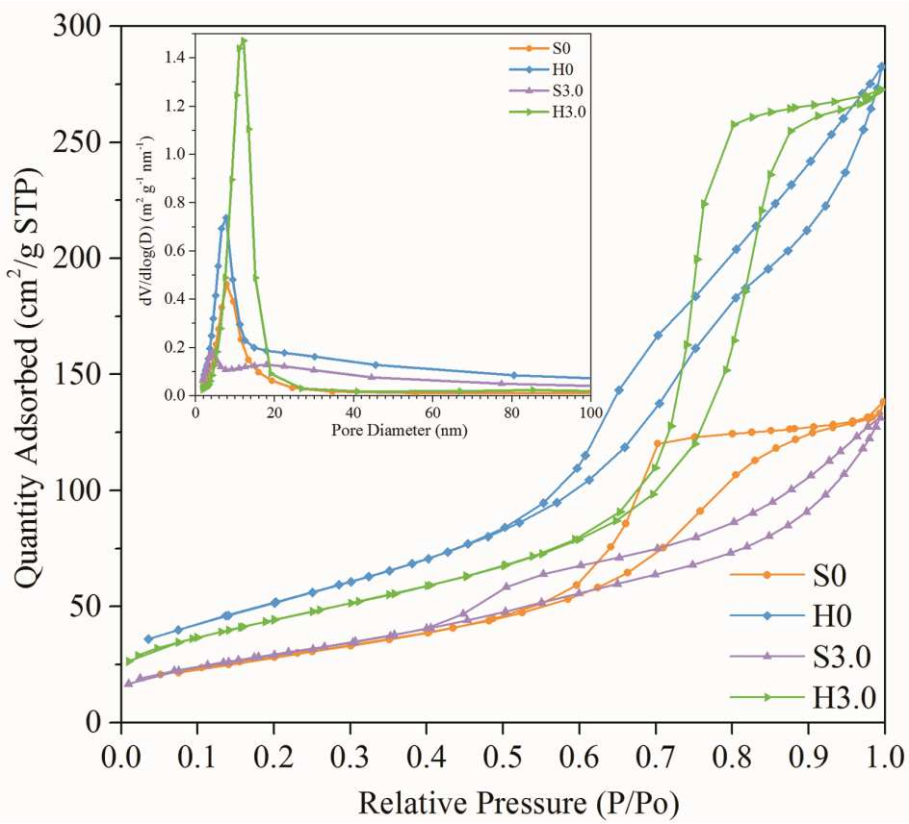

Fig. 11 N_2 adsorption-desorption isotherms and BJH pore distribution curves (inset image) of the sample S0, H0, S3.0 and H3.0

3.6 BET surface area analysis

Fig. 11 shows the N_2 adsorption-desorption isotherms and BJH pore distribution curves (inset image) of the sample S0, H0, S3.0 and H3.0. As shown in Fig. 11, N_2

adsorption-desorption isotherms of all samples belong to the typical type IV curve demonstrating the presence of mesopores in the samples. The BET surface area, pore size and pore volume value calculated by the curves were summarized in Table 2. Generally, the hydrothermally synthesized samples exhibited a larger surface area, pore size, and pore volume, which can provide more active sites. The pore size increased and the pore volume decreased with the doping of Bi ions in both samples synthesized by two methods which agreed with previous literature. [14-16] However, it should be noted that the surface area of the samples synthesized by sol-gel method change little with the increase of content of Bi ion, while the surface area of the samples synthesized by hydrothermal method decreased dramatically but was still higher than that synthesized by sol-gel method.

3.7 First principle calculations

The band structures were calculated by the Cambridge Serial Total Energy Package (CASTEP) code, as shown in Fig. 12 (near the Fermi energy level). As shown in Fig. 12(a) and (d), the band gaps of undoped anatase TiO_2 with different size were 2.17 eV ($2 \times 2 \times 2$) and 2.19 eV ($3 \times 2 \times 1$), respectively, which is smaller than that of the experimental value (3.20 eV) due to the choice of exchange-correlation energy. It should be noted that different sizes of supercells would influence the band gap of the band structure, but they had a similar curve shape and the conduction bands (CBs) were also close to Fermi energy level (0 eV). Compared with Fig. 12(a), (d) and Fig. 12(b), (e), it can be seen that the oxygen vacancy made the conduction band and valence band move negatively, which made the Fermi energy level lie in the conduction band. At the same time, the degree of negative shift of the valence band was greater than that of the conduction band, which made the band gap slightly increased. Although the existence of oxygen vacancy can become the capturing centre of photogenerated electron-hole pair and extend the recombination of electron and hole, it will also increase the band gap, resulting in the decrease of separation efficiency under visible light. Form Fig. 12(c) and (f), after doped one Bi ion, the band gaps of the samples were narrowed to

2.13 eV (2 × 2 × 2) and 2.14 eV (3 × 2 × 1). After doping, the valence band (VB) and the conduction band (CB) will shift negatively and the Fermi energy level will lie in the middle of the band gap. It also can be seen that there is an impurity energy level near Fermi energy level and it was closed to the conduction band (CB) about 0.57 eV (2 × 2 × 2) and 0.72 eV (3 × 2 × 1) which can act as an internal band and reduce the excitation energy (Lakshmana Reddy et al., 2016). From Fig. 12(G), the impurity energy level of Bi disappeared after doping an oxygen vacancy because the impurity energy level entered the conduction band (CB) after the negative shift of band. Though the band gap (2.15 eV) was similar to that of Bi-doped TiO_2, the disappearance of impurity band will reduce the photocatalytic efficiency of photocatalyst under visible light (Chandraboss et al., 2016; Kumar et al., 2016).

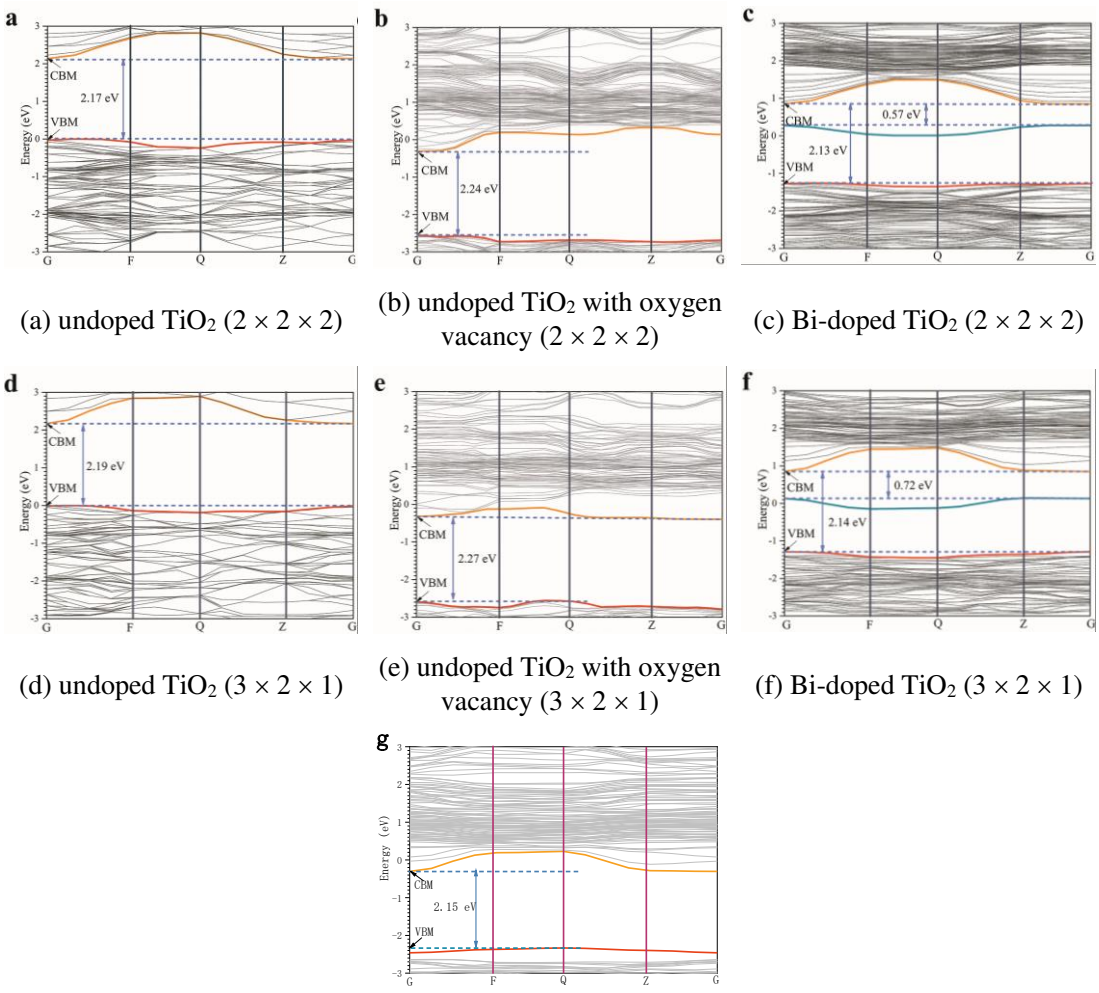

(a) undoped TiO_2 (2 × 2 × 2)

(b) undoped TiO_2 with oxygen vacancy (2 × 2 × 2)

(c) Bi-doped TiO_2 (2 × 2 × 2)

(d) undoped TiO_2 (3 × 2 × 1)

(e) undoped TiO_2 with oxygen vacancy (3 × 2 × 1)

(f) Bi-doped TiO_2 (3 × 2 × 1)

(g) Bi-doped TiO_2 with oxygen vacancy (3 × 2 × 1)

Fig. 12 Band structure near the Fermi energy level calculated by CASTEP

3.8 Photocatalytic activity study

The UV and visible light photocatalytic activity of bare TiO_2 and Bi-doped TiO_2 with different content was evaluated by the degradation of Methyl Orange (MO), as shown in Fig. 13. Under UV light, an interesting observation is that the sample H0 showed the highest MO degradation rate which may be because of the larger surface area (193.96 m^2/g) and larger band gap (2.85 eV). However, under visible light, the MO degradation rate of the sample H0 was lower than that of Bi-doped samples because fewer electrons can get excited by the visible light energy. According to the results of UV-vis DRS, doping Bi ions can narrow the band gap of samples, which can be used to explain why the MO degradation rate significantly improved under visible light. However, when the doping content of Bi ions exceeded curtain value, the MO degradation rate of the samples decreased because the too many bismuth ions would become recombination centres leading to the quick recombination of exceeded electrons.

It should be noted that the photoactivity of the samples synthesized by the hydrothermal method was higher than that synthesized by the sol-gel method of the same content of Bi ions which does not match the band gap energy results, indicating that the major factor of photodegradation may be the surface area.

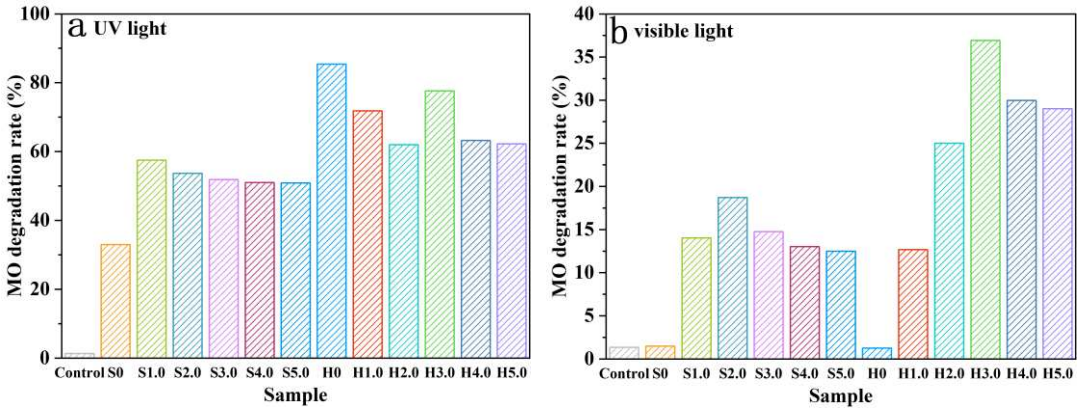

Fig. 13 Photodegradation of Methyl Orange (MO) using bare TiO_2 and Bi-doped TiO_2 under UV (a) and visible light (b) for 90 min

The NO degradation test results of modified asphalt are shown in Fig. 14. The results were consistent with those of photocatalytic degradation of MO. Generally

speaking, the photocatalytic activity of samples prepared by hydrothermal method is higher than that prepared by sol-gel method. Under UV light, the modified asphalt of H0 sample had the highest catalytic activity. Under visible light, the photocatalytic efficiency of pure titanium dioxide modified asphalt can be almost ignored. Under UV light, the degradation efficiency of H0 modified asphalt was 90.8%; under visible light, the degradation efficiency of H4.0 modified asphalt was the highest, 77.6%. A reusability experiment was carried out using H4.0 modified asphalt to examine its stability under visible light, as shown in Fig. 15. At the end of each experiment, the sample tray was taken out and washed with deionized water for three times, then air dried naturally, and then carried out the next cycle experiment. The results showed that the degradation efficiency did not fluctuate significantly after 5 cycles. Small fluctuation may be caused by measurement error and environmental fluctuation of the test chamber Although part of the photocatalyst cannot work because it was wrapped by asphalt, asphalt can fix the photocatalyst and make it play a stable role.

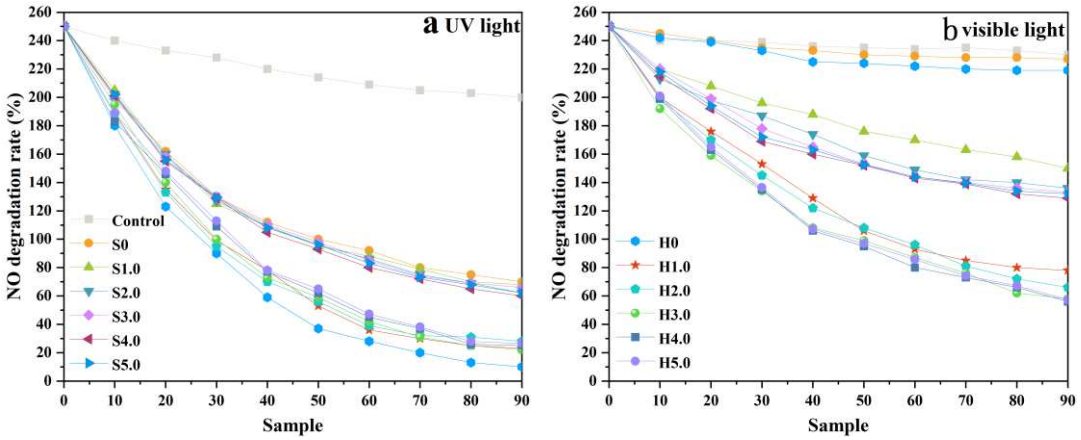

Fig. 14 Photodegradation of nitric oxide (NO) of photocatalyst modified asphalt under UV (a) and visible light (b)

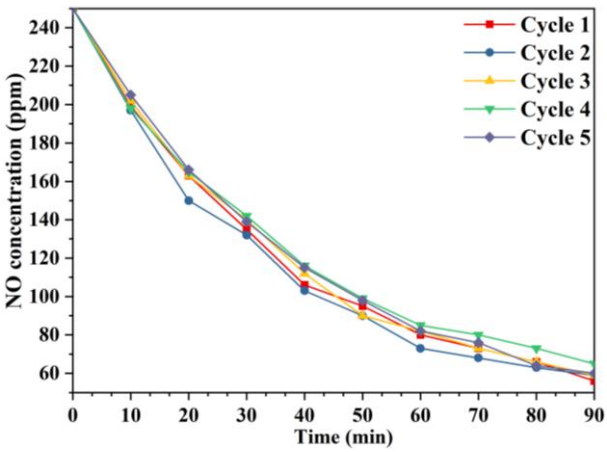

Fig. 15 Reusability investigation of the H4.0 modified asphalt

To quantitatively evaluate the photocatalytic efficiency, we conducted a kinetic analysis of nitric oxide (NO) degradation under both UV and visible light. The reaction kinetics were analyzed using the pseudo-first-order kinetic model:

$$\ln\left(\frac{C}{C_0}\right) = -kt$$

where C_0 is the initial NO concentration; C is the NO concentration at time t; k is the pseudo-first-order rate constant.

The kinetic fitting results are shown in Table 3. The results demonstrate that Bi-doped TiO_2 synthesized via the hydrothermal method (H4.0) exhibited the highest reaction rate constant under visible light, confirming its superior photocatalytic activity. The enhanced kinetics can be attributed to its larger surface area, reduced band gap, and improved charge separation efficiency. Additionally, the kinetic data further corroborate the trends observed in the photocatalytic NO degradation experiments (Fig. 14), reinforcing the effectiveness of Bi-doped TiO_2 in asphalt applications.

Table 3 Pseudo-first-order kinetic parameters for NO photodegradation under UV and visible light

Sample	UV Light		Visible Light	
	k (min^{-1})	R^2	k (min^{-1})	R^2
Control	0.00234	0.97767	0.00050	0.91688
S0	0.01280	0.96165	0.00089	0.86624
S1.0	0.01334	0.94923	0.00471	0.99247
S2.0	0.01423	0.97201	0.00590	0.96927
S3.0	0.01379	0.96627	0.00629	0.93849
S4.0	0.01488	0.97520	0.00612	0.94196
S5.0	0.01438	0.97141	0.00610	0.93576
H0	0.03676	0.99763	0.00132	0.88636

H1.0	0.02774	0.97942	0.01272	0.96427
H2.0	0.02458	0.96009	0.01399	0.99484
H3.0	0.02799	0.99146	0.01494	0.99051
H4.0	0.02639	0.99093	0.01537	0.98095
H5.0	0.02590	0.99063	0.01526	0.98467

The degradation of nitric oxide (NO) under photocatalytic conditions follows a series of redox reactions facilitated by the Bi-doped titanium dioxide (Bi-TiO_2) system. When exposed to solar light, TiO_2 absorbs photons, exciting electrons from the valence band to the conduction band, creating electron-hole pairs. The presence of bismuth introduces impurity energy levels, which improve charge separation and enhance the absorption of visible light.

The photogenerated electrons in the conduction band interact with molecular oxygen to form superoxide radicals, which contribute to NO oxidation. Simultaneously, the photogenerated holes in the valence band react with surface hydroxyl groups or water molecules to generate hydroxyl radicals. These reactive oxygen species actively oxidize NO into nitrogen dioxide (NO_2), which subsequently undergoes further oxidation to form nitrate (NO_3^-). The produced nitrate ions are either adsorbed onto the catalyst surface or dissolved in the surrounding medium. Overall, the Bi doping enhances photocatalytic efficiency by improving charge carrier separation and increasing active sites, leading to a more efficient and stable degradation of NO under both UV and visible light conditions.

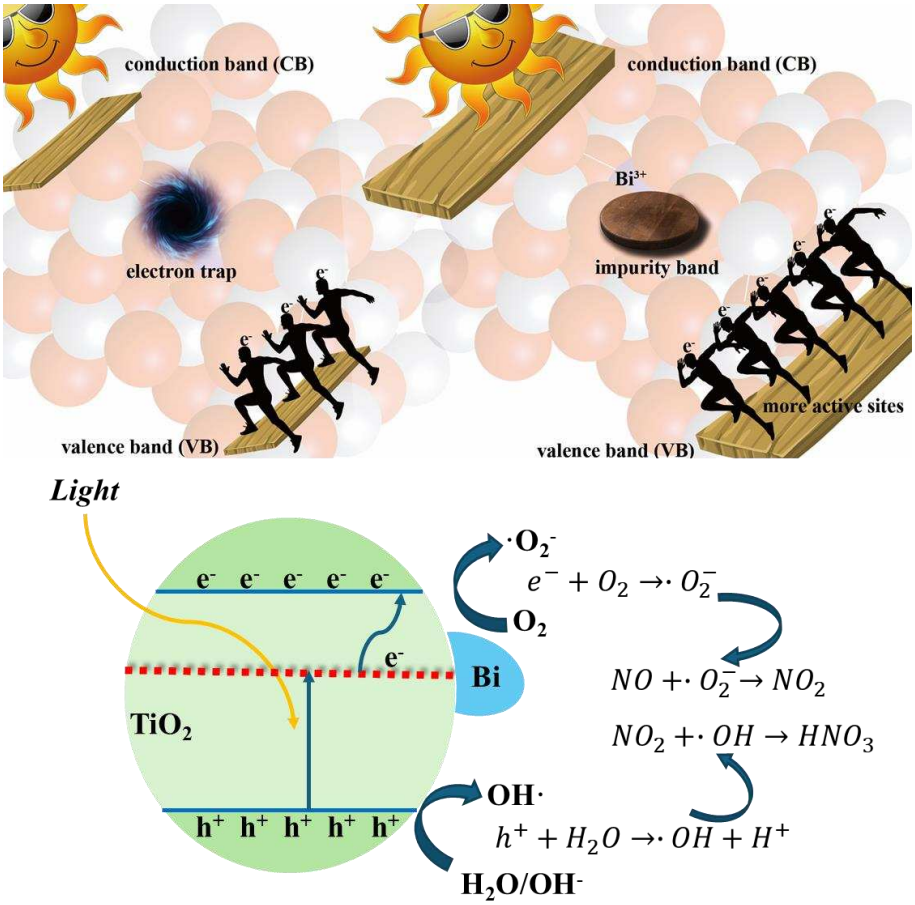

Fig. 16 Schematic illustration of the NO photodegradation mechanism over Bi-doped TiO_2

4. Discussion

The photocatalytic performance of Bi-doped TiO_2 was strongly influenced by the preparation method, which affected particle size, crystallinity, and surface area. Under UV light, hydrothermal TiO_2 exhibited superior photocatalytic activity compared to sol-gel TiO_2, primarily due to its smaller particle size, larger surface area, and fewer structural defects. In contrast, sol-gel-prepared TiO_2 suffered from particle agglomeration, which reduced its available surface area and light absorption efficiency. However, Bi doping introduced structural defects, which enhanced UV absorbance and affected photocatalytic performance.

Under visible light, Bi doping played a more critical role by inducing band gap narrowing and impurity states, facilitating electron excitation and improving photocatalytic efficiency. The valence band (VB) and conduction band (CB) were shifted negatively, allowing for better utilization of visible light. However, excessive

defects, particularly oxygen vacancies, negatively impacted performance by increasing charge recombination rates. Theoretical calculations confirmed that while Bi doping reduced the band gap, excessive oxygen vacancies led to an energy level shift, thereby reducing photocatalytic efficiency under visible light.

Structural analysis further indicated that surface area, pore size, and crystallinity were key factors influencing photocatalytic performance. Hydrothermal synthesis yielded larger crystallite sizes and fewer defects, while sol-gel synthesis produced smaller crystallites with higher defect concentrations. Despite the smaller band gap of sol-gel samples, their higher defect density acted as recombination centers, ultimately limiting photocatalytic performance.

In summary, compared to previous studies, this work offers a methodical comparison of two synthesis strategies (sol-gel and hydrothermal) and systematically links their influence on the physicochemical structure of Bi-doped TiO_2 to its photocatalytic performance. By integrating theoretical modeling with experimental analysis, we provide a unified framework for understanding how Bi doping and defect engineering affect band structure and activity under both UV and visible light. This study also presents the demonstration of optimized Bi-TiO_2 photocatalysts embedded in asphalt materials, achieving validated NO degradation performance under dual light sources. This work not only advances material-level understanding but also bridges the gap between catalyst design and real-world application, offering a methodological foundation for the future development of photocatalytic pavement systems aimed at mitigating urban air pollution.

5. Conclusions and outlook

This study successfully synthesized Bi-doped TiO_2 photocatalysts via hydrothermal and sol-gel methods and systematically evaluated their photocatalytic performance for NO degradation in asphalt applications. Key findings are summarized as follows:

(1) The hydrothermal method produced photocatalysts with higher surface area, larger crystallite size, and fewer structural defects, resulting in superior photocatalytic efficiency under visible light. In contrast, sol-gel-prepared samples exhibited more defects, leading to enhanced visible-light absorption but increased electron-hole recombination, reducing overall efficiency.

(2) Bi incorporation effectively reduced the band gap and extended visible-light absorption. However, excessive doping induced oxygen vacancies, which acted as recombination centers, offsetting the benefits of band gap narrowing.

(3) DFT calculations confirmed the red shift in optical absorption due to Bi doping, while excessive oxygen vacancies counteracted this effect by increasing the band gap, thereby diminishing visible-light-driven photocatalysis.

(4) Bi-doped TiO_2-modified asphalt demonstrated high NO degradation efficiency, with H4.0 achieving the best performance under visible light and exhibiting stable reusability, underscoring its potential for real-world urban air pollution mitigation.

While this study provides critical insights into Bi-doped TiO_2 photocatalysts for asphalt-based NO degradation, further research is required to optimize long-term performance and real-world applicability:

(1) Investigating the long-term effects of Bi-doped TiO_2 on asphalt durability and aging resistance to ensure structural integrity under real-world conditions.

(2) Determining the optimal photocatalyst-to-asphalt ratio and surface modification strategies to balance photocatalytic efficiency with mechanical stability.

(3) Conducting large-scale field trials to assess real-world NO_x degradation efficiency, considering variables such as traffic density, pollutant concentration, and environmental factors.

These future directions will contribute to the practical deployment of photocatalytic asphalt pavements, offering an innovative and sustainable approach to mitigating urban air pollution.

References

Adhikary, J., Chakraborty, P., Das, B., Datta, A., Dash, S. K., Roy, S., Chen, J.-W., & Chattopadhyay, T. (2015). Preparation and characterization of ferromagnetic nickel oxide nanoparticles from three different precursors: Application in drug delivery. *RSC Advances*, *5*(45), 35917–35928. https://doi.org/10.1039/C5RA00642B

Ahmad, I., Zou, Y., Yan, J., Liu, Y., Shukrullah, S., Naz, M. Y., Hussain, H., Khan, W. Q., & Khalid, N. R. (2023). Semiconductor photocatalysts: A critical review highlighting the various strategies to boost the photocatalytic performances for diverse applications. *Advances in Colloid and Interface Science*, *311*, 102830. https://doi.org/10.1016/j.cis.2022.102830

Alimard, P., Gong, C., Itskou, I., & Kafizas, A. (2024). Achieving high photocatalytic NOx removal activity using a Bi/BiOBr/TiO2 composite photocatalyst. *Chemosphere*, *368*, 143728. https://doi.org/10.1016/j.chemosphere.2024.143728

Baghitabar, K., Jamshidi, M., & Ghamarpoor, R. (2023). Exfoliation, hydroxylation and silanization of two-dimensional (2D) montmorillonites (MMTs) and evaluation of the effects on tire rubber properties. *Polymer Testing*, *129*, 108265. https://doi.org/10.1016/j.polymertesting.2023.108265

Ballari, M. M., Hunger, M., Hüsken, G., & Brouwers, H. J. H. (2010a). Modelling and experimental study of the NOx photocatalytic degradation employing concrete

621 pavement with titanium dioxide. *Catalysis Today*, *151*(1), 71–76. Q1/Q2.
622 https://doi.org/10.1016/j.cattod.2010.03.042
623 Ballari, M. M., Hunger, M., Hüsken, G., & Brouwers, H. J. H. (2010b). NOx
624 photocatalytic degradation employing concrete pavement containing titanium
625 dioxide. *Applied Catalysis B: Environmental*, *95*(3), 245–254. Q1.
626 https://doi.org/10.1016/j.apcatb.2010.01.002
627 Barkouch, H., Bessbousse, H., Amar, M., Bouzzine, S. M., Hamidi, M., El Mhammedi,
628 M. A., & Alaoui, O. T. (2023). Bismuth-doped TiO2 enable solar photocatalytic
629 water treatment. *Optical Materials*, *146*, 114507.
630 https://doi.org/10.1016/j.optmat.2023.114507
631 Cao, X., Yang, X., Li, H., Huang, W., & Liu, X. (2017). Investigation of Ce-TiO2
632 photocatalyst and its application in asphalt-based specimens for NO degradation.
633 *Construction and Building Materials*, *148*, 824–832.
634 https://doi.org/10.1016/j.conbuildmat.2017.05.095
635 Chandraboss, V. L., Kamalakkannan, J., & Senthilvelan, S. (2016). Synthesis of
636 activated charcoal supported Bi-doped TiO2 nanocomposite under solar light
637 irradiation for enhanced photocatalytic activity. *Applied Surface Science*, *387*,
638 944–956. https://doi.org/10.1016/j.apsusc.2016.06.110
639 Chen, D., Cheng, Y., Zhou, N., Chen, P., Wang, Y., Li, K., Huo, S., Cheng, P., Peng, P.,
640 Zhang, R., Wang, L., Liu, H., Liu, Y., & Ruan, R. (2020). Photocatalytic
641 degradation of organic pollutants using TiO2-based photocatalysts: A review.

642 *Journal of Cleaner Production*, *268*, 121725.
643 https://doi.org/10.1016/j.jclepro.2020.121725
644 Debelu, D., Mengistu, D. A., Aschalew, A., Mengistie, B., & Deriba, W. (2024). Global
645 public health implications of traffic related air pollution: Systematic review.
646 *Environmental Health Insights*, *18*, 11786302241272403.
647 https://doi.org/10.1177/11786302241272403
648 Dylla, H., Asadi, S., Hassan, M., & Mohammad, L. N. (2013). Evaluating
649 photocatalytic asphalt pavement effectiveness in real-world environments
650 through developing models: A statistical and kinetic study. *Road Materials and*
651 *Pavement Design*, *14*(sup2), 92–105.
652 https://doi.org/10.1080/14680629.2013.812839
653 Dylla, H., Hassan, M. M., Mohammad, L. N., Rupnow, T., & Wright, E. (2010).
654 Evaluation of Environmental Effectiveness of Titanium Dioxide Photocatalyst
655 Coating for Concrete Pavement. *Transportation Research Record*, *2164*(1), 46–
656 51. https://doi.org/10.3141/2164-06
657 Eftekharipour, F., Jamshidi, M., & Ghamarpoor, R. (2023). Fabricating core-shell of
658 silane modified nano ZnO; effects on photocatalytic degradation of benzene in
659 air using acrylic nanocomposite. *Alexandria Engineering Journal*, *70*, 273–288.
660 https://doi.org/10.1016/j.aej.2023.02.047
661 Estrada-Flores, S., Pérez-Berumen, C. M., Flores-Guia, T. E., García-Cerda, L. A.,
662 Rodríguez-Hernández, J., Esquivel-Castro, T. A., & Martínez-Luévanos, A.

(2022). Mechanosynthesis of mesoporous Bi-doped TiO2: The effect of bismuth doping and ball milling on the crystal structure, optical properties, and photocatalytic activity. *Crystals*, *12*(12), Article 12. https://doi.org/10.3390/cryst12121750

Gao, J., Woodward, A., Vardoulakis, S., Kovats, S., Wilkinson, P., Li, L., Xu, L., Li, J., Yang, J., Li, J., Cao, L., Liu, X., Wu, H., & Liu, Q. (2017). Haze, public health and mitigation measures in China: A review of the current evidence for further policy response. *Science of the Total Environment*, *578*, 148–157. https://doi.org/10.1016/j.scitotenv.2016.10.231

Gatou, M.-A., Syrrakou, A., Lagopati, N., & Pavlatou, E. A. (2024). Photocatalytic TiO2-based nanostructures as a promising material for diverse environmental applications: A review. *Reactions*, *5*(1), Article 1. https://doi.org/10.3390/reactions5010007

Ghamarpoor, R., Jamshidi, M., & Allawi Kadhim Alhaeehm, Z. (2024). Synthesis of hybrid/superhydrophobic coupling agent grafted nano SiO2 and its use in fabrication of rubber nanocomposite with outstanding oil/water separation capability. *Results in Engineering*, *22*, 102270. https://doi.org/10.1016/j.rineng.2024.102270

Ghasemi, F., Jamshidi, M., & Ghamarpoor, R. (2024). Preparation of a rubber nanocomposite for oil/water separation using surface functionalized/silanized carbon black nanoparticles. *Water Resources and Industry*, *32*, 100268.

https://doi.org/10.1016/j.wri.2024.100268

Gul, I., Sayed, M., Shah, N. S., Ali Khan, J., Polychronopoulou, K., Iqbal, J., & Rehman, F. (2020). Solar light responsive bismuth doped titania with Ti3+ for efficient photocatalytic degradation of flumequine: Synergistic role of peroxymonosulfate. *Chemical Engineering Journal*, *384*, 123255. https://doi.org/10.1016/j.cej.2019.123255

Hassan, M. M., Dylla, H., Mohammad, L. N., & Rupnow, T. (2010). Evaluation of the durability of titanium dioxide photocatalyst coating for concrete pavement. *Construction and Building Materials*, *24*(8), 1456–1461. Q1. https://doi.org/10.1016/j.conbuildmat.2010.01.009

Hassan, M., Mohammad, L. N., Asadi, S., Dylla, H., & Cooper, S. (2013). Sustainable Photocatalytic Asphalt Pavements for Mitigation of Nitrogen Oxide and Sulfur Dioxide Vehicle Emissions. *Journal of Materials in Civil Engineering*, *25*(3), 365–371. https://doi.org/10.1061/(ASCE)MT.1943-5533.0000613

He, C., & Jiang, W. (2024). Research on particle size distribution and composition of road deposit dust in xi'an: From the perspective of non-exhaust emissions. *Journal of Cleaner Production*, *470*, 143269. https://doi.org/10.1016/j.jclepro.2024.143269

He, C., Jiang, W., Wang, T., Yuan, D., & Sha, A. (2024). The evolution of tire-road wear particles and road surface texture under rolling friction. *Construction and Building Materials*, *447*, 138167.

https://doi.org/10.1016/j.conbuildmat.2024.138167

Hou, L.-R., Yuan, C.-Z., & Peng, Y. (2007). Synthesis and photocatalytic property of SnO2/TiO2 nanotubes composites. *Journal of Hazardous Materials*, *139*(2), 310–315. Q1. https://doi.org/10.1016/j.jhazmat.2006.06.035

Hu, Z., Xu, T., Liu, P., & Oeser, M. (2021). Developed photocatalytic asphalt mixture of open graded friction course for degrading vehicle exhaust. *Journal of Cleaner Production*, *279*, 123453. https://doi.org/10.1016/j.jclepro.2020.123453

Hüsken, G., Hunger, M., & Brouwers, H. J. H. (2009). Experimental study of photocatalytic concrete products for air purification. *Building and Environment*, *44*(12), 2463–2474. Q1/Q2. https://doi.org/10.1016/j.buildenv.2009.04.010

Jiang, W., Wang, T., Yuan, D., Sha, A., Zhang, S., Zhang, Y., Xiao, J., & Xing, C. (2024). Available solar resources and photovoltaic system planning strategy for highway. *Renewable and Sustainable Energy Reviews*, *203*, 114765. https://doi.org/10.1016/j.rser.2024.114765

Jin, J., Xiao, T., Tan, Y., Zheng, J., Liu, R., Qian, G., Wei, H., & Zhang, J. (2018). Effects of TiO2 pillared montmorillonite nanocomposites on the properties of asphalt with exhaust catalytic capacity. *Journal of Cleaner Production*, *205*, 339–349. https://doi.org/10.1016/j.jclepro.2018.08.251

Khan, J. A., Sayed, M., Shah, N. S., Khan, S., Zhang, Y., Boczkaj, G., Khan, H. M., & Dionysiou, D. D. (2020). Synthesis of eosin modified TiO2 film with co-exposed {001} and {101} facets for photocatalytic degradation of para-

aminobenzoic acid and solar H2 production. *Applied Catalysis B: Environmental*, *265*, 118557. https://doi.org/10.1016/j.apcatb.2019.118557

Komaraiah, D., Radha, E., Kalarikkal, N., Sivakumar, J., Ramana Reddy, M. V., & Sayanna, R. (2019). Structural, optical and photoluminescence studies of sol-gel synthesized pure and iron doped TiO2 photocatalysts. *Ceramics International*, *45*(18, Part B), 25060–25068. https://doi.org/10.1016/j.ceramint.2019.03.170

Kumar, M. K., Bhavani, K., Srinivas, B., Kumar, S. N., Sudhakar, M., Naresh, G., & Venugopal, A. (2016). Nano structured bismuth and nitrogen co-doped TiO2 as an efficient light harvesting photocatalyst under natural sunlight for the production of H2 by H2O splitting. *Applied Catalysis A: General*, *515*, 91–100. https://doi.org/10.1016/j.apcata.2016.01.009

Lakshmana Reddy, N., Krishna Reddy, G., Mahaboob Basha, K., Krishna Mounika, P., & Shankar, M. V. (2016). Highly efficient hydrogen production using Bi2O3/TiO2 nanostructured photocatalysts under led light irradiation. *Materials Today Proceedings*, *3*(6), 1351–1358. https://doi.org/10.1016/j.matpr.2016.04.014

Li, L., Tian, H.-W., Meng, F.-L., Hu, X.-Y., Zheng, W.-T., & Sun, C. Q. (2014). Defects improved photocatalytic ability of TiO2. *Applied Surface Science*, *317*, 568–572. https://doi.org/10.1016/j.apsusc.2014.08.078

Li, X., Wang, F., You, L., Wu, S., Yang, C., Zhang, L., & Maria Barbieri, D. (2023). A

review on photocatalytic asphalt pavement designed for degradation of vehicle exhausts. *Transportation Research Part D Transport and Environment*, *115*, 103605. https://doi.org/10.1016/j.trd.2023.103605

Liu, W., Wang, S., Zhang, J., & Fan, J. (2015). Photocatalytic degradation of vehicle exhausts on asphalt pavement by TiO2/rubber composite structure. *Construction and Building Materials*, *81*, 224–232. https://doi.org/10.1016/j.conbuildmat.2015.02.034

Lv, K., Zuo, H., Sun, J., Deng, K., Liu, S., Li, X., & Wang, D. (2009). (Bi, C and N) codoped TiO2 nanoparticles. *Journal of Hazardous Materials*, *161*(1), 396–401. https://doi.org/10.1016/j.jhazmat.2008.03.111

Ma, J., Chu, J., Qiang, L., & Xue, J. (2012). Synthesis and structural characterization of novel visible photocatalyst Bi–TiO2/SBA-15 and its photocatalytic performance. *RSC Advances*, *2*(9), 3753–3758. https://doi.org/10.1039/C2RA01199A

Ma, L., Huang, C., Li, X., An, X., Li, J., Zou, L., Zhu, X., Yuan, C., Dai, X., Zhou, Y., Zhu, X., & Tian, C. (2025). In situ synthesis of mesoporous TiO2 doped with bismuth single atoms for tunable photocatalytic degradation of formaldehyde. *Separation and Purification Technology*, *354*, 128635. https://doi.org/10.1016/j.seppur.2024.128635

Mishra, S., Chakinala, N., Sethia, G., Chakinala, A. G., & Surolia, P. K. (2024). Enhanced photocatalytic performance of Bi-doped TiO2 under sunlight and UV

light: Mechanistic insights and comparative analysis. *Photochemical & Photobiological Sciences*, *23*(8), 1495–1507. https://doi.org/10.1007/s43630-024-00609-3

Narindri Rara Winayu, B., Tsai, Y.-Y., & Chu, H. (2022). Enhancement of formaldehyde removal by graphene, S, and N doping on TiO2 nanocomposite photocatalyst. *Journal of Physics and Chemistry of Solids*, *170*, 110961. Q2. https://doi.org/10.1016/j.jpcs.2022.110961

Nowotny, J., Alim, M. A., Bak, T., Idris, M. A., Ionescu, M., Prince, K., Sahdan, M. Z., Sopian, K., Teridi, M. A. M., & Sigmund, W. (2015). Defect chemistry and defect engineering of TiO2-based semiconductors for solar energy conversion. *Chemical Society Reviews*, *44*(23), 8424–8442. https://doi.org/10.1039/C4CS00469H

Poon, C. S., & Cheung, E. (2007). NO removal efficiency of photocatalytic paving blocks prepared with recycled materials. *Construction and Building Materials*, *21*(8), 1746–1753. Q1. https://doi.org/10.1016/j.conbuildmat.2006.05.018

Qi, W., Zhang, F., An, X., Liu, H., & Qu, J. (2019). Oxygen vacancy modulation of {010}-dominated TiO2 for enhanced photodegradation of sulfamethoxazole. *Catalysis Communications*, *118*, 35–38. https://doi.org/10.1016/j.catcom.2018.09.014

Rahman, M. A., Bazargan, S., Srivastava, S., Wang, X., Abd-Ellah, M., Thomas, J. P., Heinig, N. F., Pradhan, D., & Leung, K. T. (2015). Defect-rich decorated TiO2

nanowires for super-efficient photoelectrochemical water splitting driven by visible light. *Energy & Environmental Science*, *8*(11), 3363–3373. https://doi.org/10.1039/C5EE01615K

Samsudin, E. M., & Abd Hamid, S. B. (2017). Effect of band gap engineering in anionic-doped TiO2 photocatalyst. *Applied Surface Science*, *391*, 326–336. https://doi.org/10.1016/j.apsusc.2016.07.007

Sangpour, P., Hashemi, F., & Moshfegh, A. Z. (2010). Photoenhanced Degradation of Methylene Blue on Cosputtered M:TiO2 (M = Au, Ag, Cu) Nanocomposite Systems: A Comparative Study. *The Journal of Physical Chemistry C*, *114*(33), 13955–13961. https://doi.org/10.1021/jp910454r

Sayed, M., Ren, B., Ali, A. M., Al-Anazi, A., Nadagouda, M. N., Ismail, A. A., & Dionysiou, D. D. (2022). Solar light induced photocatalytic activation of peroxymonosulfate by ultra-thin Ti3+ self-doped Fe2O3/TiO2 nanoflakes for the degradation of naphthalene. *Applied Catalysis B: Environmental*, *315*, 121532. https://doi.org/10.1016/j.apcatb.2022.121532

Slomski, A. (2018). Air pollution may limit health benefits of walking. *JAMA*, *319*(8), 761. https://doi.org/10.1001/jama.2018.1198

Tolan, D. A., El-Sawaf, A. K., Alhindawy, I. G., Ismael, M. H., Nassar, A. A., El-Nahas, A. M., Maize, M., Elshehy, E. A., & El-Khouly, M. E. (2023). Effect of bismuth doping on the crystal structure and photocatalytic activity of titanium oxide. *RSC Advances*, *13*(36), 25081–25092. https://doi.org/10.1039/D3RA04034H

van Veldhoven, K., Kiss, A., Keski-Rahkonen, P., Robinot, N., Scalbert, A., Cullinan, P., Chung, K. F., Collins, P., Sinharay, R., Barratt, B. M., Nieuwenhuijsen, M., Rodoreda, A. A., Carrasco-Turigas, G., Vlaanderen, J., Vermeulen, R., Portengen, L., Kyrtopoulos, S. A., Ponzi, E., Chadeau-Hyam, M., & Vineis, P. (2019). Impact of short-term traffic-related air pollution on the metabolome – results from two metabolome-wide experimental studies. *Environment International*, *123*, 124–131. https://doi.org/10.1016/j.envint.2018.11.034

Wang, D., Leng, Z., Hueben, M., Oeser, M., & Steinauer, B. (2016). Photocatalytic pavements with epoxy-bonded TiO2-containing spreading material. *Construction and Building Materials*, *107*, 44–51. https://doi.org/10.1016/j.conbuildmat.2015.12.164

Wang, D., Leng, Z., Yu, H., Hueben, M., Kollmann, J., & Oeser, M. (2017). Durability of epoxy-bonded TiO2-modified aggregate as a photocatalytic coating layer for asphalt pavement under vehicle tire polishing. *Wear*, *382*, 1–7. https://doi.org/10.1016/j.wear.2017.04.004

Wang, H., Wu, Z., Zhao, W., & Guan, B. (2007). Photocatalytic oxidation of nitrogen oxides using TiO2 loading on woven glass fabric. *Chemosphere*, *66*(1), 185–190. Q1. https://doi.org/10.1016/j.chemosphere.2006.04.071

Wang, T., Riccardi, C., & Jiang, W. (2025). From waste to sustainable pavement: Rejuvenation of asphalt binder using waste engine oil residue and crumb rubber. *Chemical Engineering Journal*, *505*, 159523.

https://doi.org/10.1016/j.cej.2025.159523

Wei, Z., Liu, J., & Shangguan, W. (2020). A review on photocatalysis in antibiotic wastewater: Pollutant degradation and hydrogen production. *Chinese Journal of Catalysis*, *41*(10), 1440–1450. https://doi.org/10.1016/S1872-2067(19)63448-0

Xu, Y., Jin, R., Hu, L., Li, B., Chen, W., Shen, J., Wu, P., & Fang, J. (2020). Studying the mix design and investigating the photocatalytic performance of pervious concrete containing TiO2-Soaked recycled aggregates. *Journal of Cleaner Production*, *248*, 119281. https://doi.org/10.1016/j.jclepro.2019.119281